AGU PUBLICATIONS

JGR

Journal of Geophysical Research: Oceans

RESEARCH ARTICLE

10.1002/2015JC011044

Key Points:
- Hurricane rain's effect on SAR backscatter is studied
- A composite backscattering model was developed to understand the mechanism
- Radar model is validated with C-band VV polarization SAR data

Correspondence to:
X. Li,
xiaofeng.li@noaa.gov

Citation:
Zhang, G., X. Li, W. Perrie, B. Zhang, and L. Wang (2016), Rain effects on the hurricane observations over the ocean by C-band Synthetic Aperture Radar, *J. Geophys. Res. Oceans*, *121*, 14–26, doi:10.1002/2015JC011044.

Received 12 JUN 2015
Accepted 6 DEC 2015
Accepted article online 13 DEC 2015
Published online 7 JAN 2016

Rain effects on the hurricane observations over the ocean by C-band Synthetic Aperture Radar

Guosheng Zhang[1,2], Xiaofeng Li[3], William Perrie[2], Biao Zhang[4,5], and Lei Wang[6]

[1]International Center for Marine Studies, Shanghai Ocean University, Shanghai, China, [2]Fisheries and Oceans Canada, Bedford Institute of Oceanography, Dartmouth, Nova Scotia, Canada, [3]GST, National Oceanic and Atmospheric Administration/NESDIS, College Park, Maryland, USA, [4]School of Marine Sciences, Nanjing University of Information Science and Technology, Nanjing, China, [5]Jiangsu Engineering Technology Research Center of Marine Environment Detection, Nanjing, China, [6]School of Atmospheric Sciences, Nanjing University, Nanjing, China

Abstract A composite radar scattering model composed of the atmosphere radiative transfer model, and the ocean surface Bragg wave theory is developed to analyze the impact of hurricane rain on the normalized radar-backscatter cross section (NRCS) measured in the VV and cross-polarized C-band Synthetic Aperture Radar (SAR) channels. The model results are validated against SAR and SFMR measured wind speeds and rain rates for two hurricane cases. The contribution of rain to the NRCS is backscatter from two parts: the atmosphere column and the ocean surface. In the atmosphere, microwave attenuation and the rain-induced volume backscattering are simulated by the model. We find that the impact of raindrops in the atmosphere is almost negligible for the VV polarization, but important for the cross polarization. On the ocean surface, comparisons between our model and other existing models without rain lead to the conclusion that the VV polarization NRCS can be simulated reasonably well without considering the non-Bragg scattering mechanisms. Similar to the wave breaking mechanism, the microwave diffraction on the craters, crowns, and stalks, produced by rain drops, is also negligible for VV polarization. However, the non-Bragg scattering is important for the cross-polarized NRCS simulations. Finally, we performed simulations to understand the VV-polarized NRCS behavior under different wind speeds at various rain rates.

1. Introduction

Hurricanes or typhoons (all storms are referred to as hurricanes hereafter) have been frequently observed in spaceborne Synthetic Aperture Radar (SAR) images since the first SAR image became available in 1978 [*Fu and Holt*, 1982]. With the advantage of its high spatial resolution, relative large spatial coverage (especially with ScanSAR technology) and the capability of imaging the imprint of hurricanes on the ocean surface under almost all-weather conditions, the SAR instrument is suitable for detailed hurricane observations over the sea surface. Therefore, SAR images were adopted by many scientists to understand hurricane eye characteristics [*Du and Vachon*, 2003; *Jin et al*., 2014], morphology [*Friedman and Li*, 2000; *Li et al*., 2013], tracks [*Zheng et al*., 2015], intensity [*Reppucci et al*., 2010; *Zhang et al*., 2014], winds [*Zhang and Perrie*, 2012; *Zhou et al*., 2013; *Li*, 2015], and swell waves [*Li et al*., 2002]. However, rainfall associated with hurricanes was not addressed quantitatively in these studies. In general, rain has two significant effects on the normalized radar-backscatter cross section (NRCS) of the SAR: (1) raindrops induce volumetric scattering and attenuation in the atmosphere and (2) rain alters the roughness of the ocean surface. The aim of this study is to understand each of these mechanisms under hurricane conditions.

On the ocean surface, a NRCS model including the rain damping effect on the wind-induced waves, and the rain enhanced ring wave spectra, was developed by *Contreras and Plant* [2006]. They added the two rain effects to a semiempirical wind wave spectrum model developed by *Kudryavtsev et al*. [2003] (hereafter denoted the KHCC wave spectral model). However, the sea surface waves that satisfy Bragg resonance condition are tilted by the long waves, so the local incident angles and polarizations are altered [*Valenzuela*, 1968, 1978; *Bass et al*., 1968; *Plant*, 1990]. This tilting effect is merely dealt with by averaging over the scales of the long waves in the Bragg scattering model adopted by *Kudryavtsev et al*. [2003] and *Contreras and Plant* [2006], instead of using a probability density function (PDF) methodology. As the geometric coefficients are zeros for the cross polarizations, the averaging process over the scales of long waves cannot

simulate the cross-polarized NRCS caused by Bragg wave resonance. Recently, *Kudryavtsev et al*. [2014] simulated the NRCS due to the Bragg resonance by adopting the PDF methodology. In the atmosphere, the raindrops attenuate the radar signal, and also intensify the NRCS through volumetric scattering. These two mechanisms were simply modeled by an empirical approach by *Nie and Long* [2007] without rain effects on the ocean surface. Thereafter, a more sophisticated physics-based radiative transfer model was developed by *Xu et al*. [2015], which is shown to give comparable results to those of the simple model of *Nie and Long* [2007]. Although *Xu et al*. [2015] simply modeled ring waves generated by rain with some success there is need for improvements; the mechanisms by which rain affects the ocean surface need further study. In *Xu et al*. [2015], the rain-induced NRCS damping was not included and the ring waves' contribution was linearly added as a modulation to the empirical geophysical model function (GMF) without considering the actual physical progresses. In this study, rain's effects on the ocean surface including the rain-induced ring waves and the damping due to the wind waves were modeled by the Bragg scattering theory and the semiempirical wave spectrum. Thus, we can analyze each NRCS modulation mechanism quantitatively.

In this paper, we investigate the hurricane rain effect on C-band SAR observations in terms of mechanisms related to the ocean surface, as well as those related to the atmosphere. Our approach is to formulate a composite model to include the rain effects in the atmosphere and also, the rain effects on the ocean surface. Section 2 describes our composite model and the rationale regarding why each piece is chosen. In section 3, the model is validated using the observed rain rates, wind speeds, and C-band VV-polarization NRCSs over two hurricanes. Finally, analysis of each mechanism effect on the SAR hurricane observation and conclusions are given in sections 4 and 5, respectively.

2. The Radar Scattering Model

In this study, we build a semiempirical radar scattering model that takes into account the impacts of both sea surface wind and rain on the NRCS. The model considers the total NRCS as the summation of backscatters from both the ocean surface and the atmosphere. As shown in Figure 1, there are five modules that are needed to account for these processes: (1) the composite sea surface Bragg model given by *Valenzuela* [1978] and *Plant* [1990] for its ability to simulate quad-polarized data; (2) the wind-driven KHCC gravity wave spectrum developed by *Kudryavtsev et al*. [2003] without the rain effect; (3) the rain damping effect on the KHCC wave spectrum given by *Contreras and Plant* [2006] and *Tsimplis* [1992]; (4) the ring wave spectrum developed by *Le Méhauté* [1988]; (5) an additive model developed by *Nie and Long* [2007] for the atmospheric part. With this new composite model, the mechanisms of the rain effect on the NRCS are analyzed.

The composite Bragg model we formulated explains C-band NRCS measurements better and is less sensitive to the choice of the roughness spectral model than is the case for Ku-band measurements [*Hwang and Plant*, 2010]. Although other wind-wave spectra are probably more commonly used [*Elfouhaily et al*., 1997], the KHCC spectrum has an advantage. The main reason for choosing KHCC is that it is developed from a balance of wind input, parasitic wave generation, and wave dissipation, and therefore is convenient to modify to include the rain damping effect on the wave dissipation.

2.1. The Surface Scattering Model

The Bragg resonance theory has been developed since the 1960s [e.g., *Wright*, 1966; *Valenzuela*, 1968; *Bass et al*., 1968; *Valenzuela*, 1978; *Plant*, 1990; *Hwang et al*., 2010]. The backscatter cross-section solutions for a slightly rough patch tilted by the longer waves are as follows:

$$\begin{aligned}
\sigma_{0HH}(\theta_i) &= 16\pi k^4 \cos^4\theta_i \left| g_{HH}(\theta_i)\left(\frac{\alpha\cos\delta}{\alpha_i}\right)^2 + g_{VV}(\theta_i)\left(\frac{\sin\delta}{\alpha_i}\right)^2 \right|^2 W\left(K_{Bx}, K_{By}\right) \\
\sigma_{0VV}(\theta_i) &= 16\pi k^4 \cos^4\theta_i \left| g_{VV}(\theta_i)\left(\frac{\alpha\cos\delta}{\alpha_i}\right)^2 + g_{HH}(\theta_i)\left(\frac{\sin\delta}{\alpha_i}\right)^2 \right|^2 W\left(K_{Bx}, K_{By}\right) \\
\sigma_{0VH}(\theta_i) &= \sigma_{0HV}(\theta_i) = 16\pi k^4 \cos^4\theta_i \left(\frac{\alpha\sin\delta\cos\delta}{\alpha_i^2}\right)^2 \left| g_{VV}(\theta_i) - g_{HH}(\theta_i)\right|^2 W\left(K_{Bx}, K_{By}\right)
\end{aligned} \tag{1}$$

where k is the radar wave number, ψ and δ are the tilting angles of the long wave in the radar incident plane and perpendicular to this plane, respectively, and θ_i is the local incidence angle of the slightly rough patch:

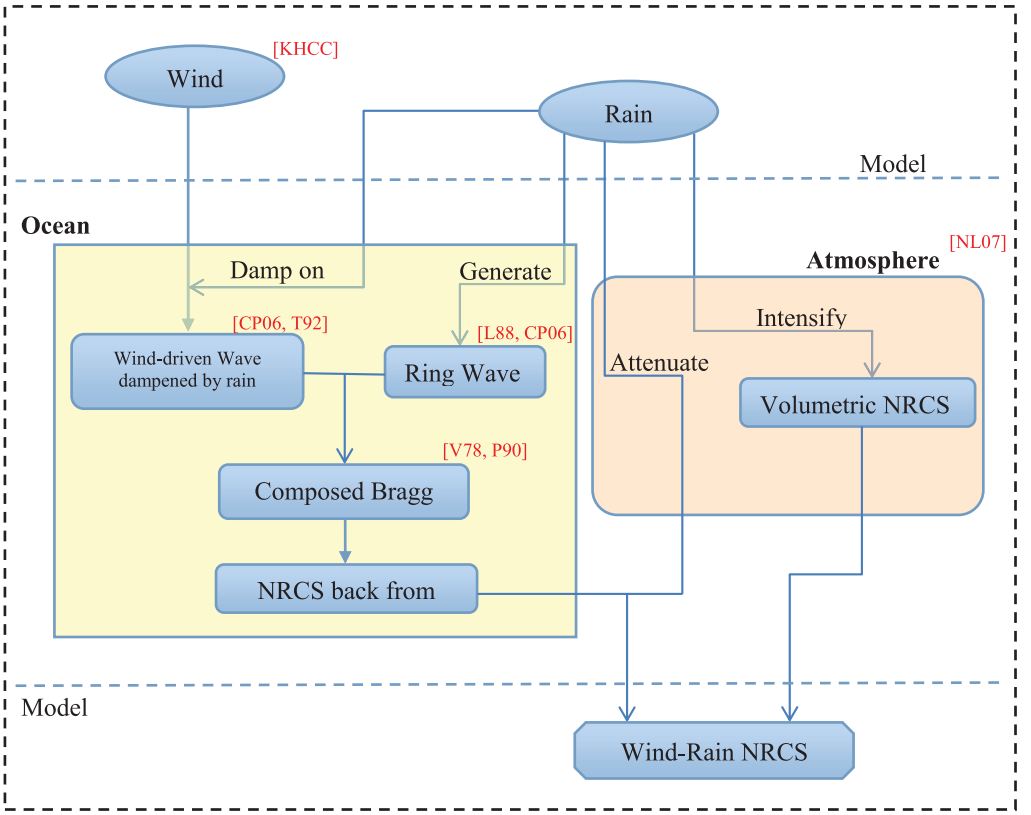

Figure 1. Outline of the model. The red abbreviations mean the references: KHCC for *Kudryavtsev et al.* [2003], CP06 for *Contreras and Plant* [2006], T92 for *Tsimplis* [1992], L88 for *Le Méhauté* [1988], V78 for *Valenzuela* [1978], P90 for *Plant* [1990], and NL07 for *Nie and Long* [2007].

$$\begin{aligned}\theta_i &= \arccos\left[\cos(\theta+\psi)\cos\delta\right]\\ \alpha_i &= \sin\theta_i\\ \alpha &= \sin(\theta+\psi),\quad \gamma=\cos(\theta+\psi)\end{aligned} \tag{2}$$

where α_i, α, and γ are parameters to simplify the formula, $W(K_{Bx}, K_{By})$ is the 2D-wave number variance spectrum, g_{VV} and g_{HH} are the Bragg scattering geometric coefficients for VV and HH polarizations:

$$\begin{aligned}g_{VV}(\theta) &= \frac{(\varepsilon_r-1)\left[\varepsilon_r\left(1+\sin^2\theta\right)-\sin^2\theta\right]}{\left[\varepsilon_r\cos\theta+\sqrt{\varepsilon_r-\sin^2\theta}\right]^2}\\ g_{HH}(\theta) &= \frac{(\varepsilon_r-1)}{\left[\cos\theta+\sqrt{\varepsilon_r-\sin^2\theta}\right]^2}\end{aligned} \tag{3}$$

and where ε_r is the relative dielectric constant of seawater. Accounting for all the surface tilting, the backscatter cross section per unit area of the sea surface is

$$\sigma_0(\theta)=\int_{-\infty}^{\infty}\int_{-\infty}^{\infty}\sigma_0(\theta_i)p(\tan\psi,\tan\delta)d(\tan\psi)d(\tan\delta) \tag{4}$$

where $p(\tan\psi, \tan\delta)$ is the joint probability density function (PDF) of the ocean surface slopes. We adopt the Gram-Charlier distribution [*Cox and Munk*, 1954] for the PDF function for p:

$$\begin{aligned}p(\tan\psi,\tan\delta) = &\frac{1}{2\pi s_c s_u}\exp\left(-\frac{\varsigma^2+\eta^2}{2}\right)\\ &\cdot\left[1-\frac{c_{21}(\varsigma^2-1)}{2}-\frac{c_{03}(\eta^3-3\eta)}{6}+\frac{c_{40}(\varsigma^4-6\varsigma^2+3)}{24}\right.\\ &\left.+\frac{c_{22}(\varsigma^2-1)(\eta^2-1)}{4}+\frac{c_{04}(\eta^4-6\eta^2+3)}{24}\right]\end{aligned} \tag{5}$$

where $\eta = \tan\psi/s_u$ and $\zeta = tan\delta/s_c$ are the normalized upwind and crosswind slope components, respectively, and s_c^2 and s_u^2 are the crosswind and upwind Mean Square Slope (MSS) variables [*Hwang et al.*, 2010]. The skewness also given by *Hwang et al.* [2010], as contained in the coefficients c_{21}, c_{40}, c_{22}, c_{04}, and c_{03}, increases with wind speed from nearly zero at low wind to $c_{21} = -0.11$, $c_{40} = 0.4$, $c_{22} = 0.1$, $c_{04} = 0.2$, and $c_{03} = -0.42$ at 14 m/s; a linear approximation is used in the implementation such that:

$$\begin{aligned} c_{21} &= -0.11U_{10}/14 \quad (U_{10} \le 14m/s) \\ c_{03} &= -0.42U_{10}/14 \quad (U_{10} \le 14m/s) \end{aligned} \tag{6}$$

With the composite Bragg theory and the wave spectrum, the backscatter from the ocean surface can be simulated for different incident angles and polarizations.

2.2. Sea Surface Wave Model

The variance spectrum for the Bragg scattering model is related to the directional wave number spectrum $S(k,\varphi)$ by:

$$W(k,\ \varphi) = S(k,\ \varphi) + S(k,\ \varphi + \pi) \tag{7}$$

Here we represent the wave spectrum with the saturation spectrum B (or the surface curvature spectrum), which is a function of the surface variance spectrum S:

$$B\left(\vec{k}\right) = k^4 S\left(\vec{k}\right) \tag{8}$$

where the rain-modulated sea surface wave spectrum B_s ranges from short gravity waves to capillary waves is:

$$B_s = B_{gc\_damped} + B_{cap} + B_{ring} \tag{9}$$

and where B_{gc_damped} is the gravity wave spectrum, damped by the precipitation, with a viscous dissipation rate for the rain-induced turbulence damping, B_{cap} is the spectrum in the gravity-capillary region, and B_{ring} is the spectrum for the rain-induced ring waves.

2.2.1. The Gravity and Gravity-Capillary Wave Spectra

For the gravity and gravity-capillary region of the spectrum, the parameterization developed by *Kudryavtsev et al.* [2003] is:

$$B_{eq}(k,\varphi) = \frac{\alpha}{2^{1/n}}\left[\beta_v(k,\varphi) + \left(\beta_v^2(k,\varphi) + 4I_{pc}(k,\varphi)/\alpha\right)^{1/2}\right]^{1/n} \tag{10}$$

where, k is the wave number, φ is the wind direction, n, α are two tuning parameters, I_{pc} is energy input due to generation of parasitic capillaries and is also a function of the effective growth rate $\beta_v(k,\varphi)$, and where effectively, $\beta_v(k,\varphi)$ is the difference between the wind growth rate $\beta(k,\varphi)$ and the viscous dissipation rate. In this model, the rain damping effect was added through the parameterization for the viscous dissipation rate. Therefore, the effective growth rate $\beta_v(k,\theta)$ may be described by:

$$\beta_v(k,\varphi) = \beta(k,\varphi) - \frac{4v_r k^2}{\omega} \tag{11}$$

where v_r is the viscosity coefficient due to the rain damping, and we adopt the rain-induced damping model developed by *Nystuen* [1990]:

$$v_r = \left(1 - e^{-2kd_{mix}}\right)\frac{v_e}{v} + e^{-2kd_{mix}} \tag{12}$$

where v_e is the rain-induced eddy viscosity. *Tsimplis* [1992] found v_e to be about 3×10^{-5} m^2/s, when rain exists, no matter how high the rain rate is. Therefore, *Contreras and Plant* [2006] described v_e with a function of the rain rate as:

$$v_e = CIv_0; \quad v_0 = \left[\left(\frac{\int_0^\infty IF(D;RR)DdD}{\rho_w d_{mix}}\right)\right]^{\frac{1}{3}} \tag{13}$$

Here l and v are differential length and velocity scales characteristic of the turbulence, $C = 0.2095$ is a constant coefficient, and IF is the energy flux into the eddy viscosity due to the rain impact:

$$IF(D;RR) = N(D;RR)\left(\frac{\pi}{12}\rho_w D^3 W^2(D)\right)W(D) \tag{14}$$

Here N is the rain drop size distribution (DSD), W is the terminal drop velocity, and $D = l$ is the diameter of the rain droplet.

For the gravity wave region, the two tuning parameters (n and α) are constants. With constant tuning parameters, B_{gc_damped} was calculated by equation (10). However, for gravity-capillary waves, the tuning parameters are functions of wave number and then the B_{cap} is computed, also using equation (10). Details of the two tuning parameters and intervals for the gravity and gravity-capillary wave numbers are the same as those of the KHCC spectrum [*Kudryavtsev et al*., 2003].

2.2.2. The Ring Wave Spectrum

The ring wave spectrum as developed by *Le Méhauté* [1988] is also adopted in our model. Given a rain drop of radius R impinging upon water, the ring wave spectrum is:

$$B_{ring}(k,RR) = \left\{\frac{64}{9}\frac{\omega^2}{g^2k^4}\int_0^\infty N(D)W^3(D)D^2\left[J_2\left(\frac{kD}{2}\right)\right]^2 dD\right\} \cdot\left\{\frac{1}{8\nu_r k^2}\left(e^{-4\nu_r k^2(0.2)} - e^{-4\nu_r k^2\tau}\right)\right\} \tag{15}$$

where ω is the wave frequency, g is the gravitational acceleration, RR is the rain rate, D is the diameter of the raindrop, $N(D)$ is the drop size distribution [*Marshall and Palmer*, 1948], $W(D)$ is the terminal fall velocity of the drop, $J_2(kD/2)$ is the second order Bessel functions of the first kind, and the maximum limit of integration τ is set to 4. The ocean surface backscatter model including the simultaneous effects of wind and rain was developed using the sea surface spectrum in equation (9) and the composite Bragg theory.

2.2.3. Results of the Sea Surface Wave Model

Figure 2 shows the saturation spectra of wind waves at various wind speeds without the rain effect. Figure 3 compares the saturation spectra with the rain effect (solid lines), rain damping (dashed line), and the wind-wave-only spectrum (dotted line) for a wind speed of 10 m/s with different rain rates. The rain effect on the waves contains wind-generated waves damped by rain and the rain-generated ring waves. Regarding the magnitude of the spectral values, although rain-affected wave spectra are higher than the wave spectra only damped by rain (by adding the ring waves), the rain-affected wave spectra are still lower than the wind-induced wave spectra. Hence, the composite rain effect on the ocean surface waves is attenuation of these waves.

2.3. Atmospheric Rain Effect on NRCS

In the atmosphere, raindrops attenuate the radar transmitting signal and also induce volume scattering. These two mechanisms compete by decreasing or increasing the NRCS, respectively. An additive model, including the rain's effect on the NRCS in the atmosphere is given by *Nie and Long* [2007]:

$$\sigma_m = \sigma_{surf}\alpha_{atm} + \sigma_{atm} \tag{16}$$

where σ_m is the total NRCS received by radar, σ_{surf} is the backscatter from the ocean surface, α_{atm} is the rain-induced atmospheric attenuation, and σ_{atm} is the atmospheric volume backscatter.

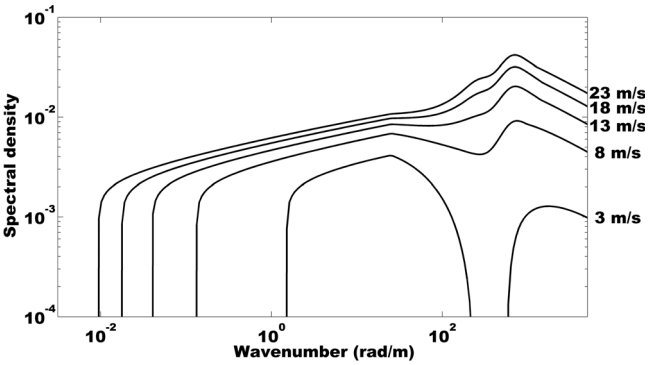

Figure 2. Model saturation spectra of short wind waves at various wind speeds without the rain effect: 3–23 m/s from lower to upper curves with the resolution of 5 m/s.

3. Validation of the Composite Model

To validate the accuracy of this wind-rain model, data sets of C-band VV-polarized NRCSs, wind speeds, and rain rates over two hurricanes were investigated.

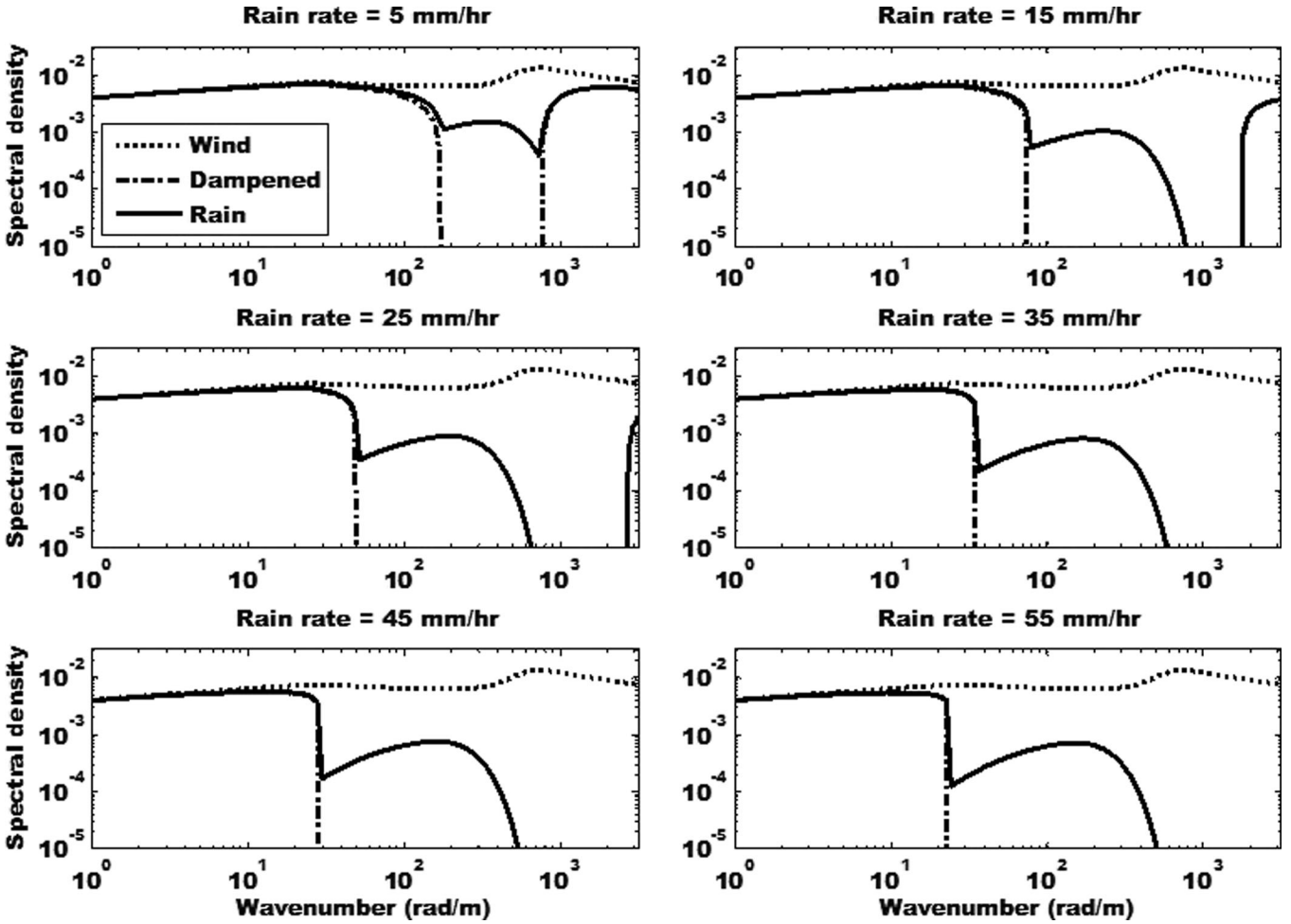

Figure 3. Saturation spectra for a wind speed of 10 m/s with different rain rates: wind wave spectrum (dotted), damped wind wave spectrum (dashed), and damped wind wave spectrum with additive ring wave spectrum (solid).

3.1. Wide-Swath SAR Data

We have acquired two *Envisat* SAR images over Hurricane Gustav (03:56 UTC, 1 September 2008) and Hurricane Ike (04:23 UTC, 13 September 2008) from the European Space Agency (ESA). The SAR images are wide swath mode (WSM) with a medium resolution of 150 m and a swath width of 405 km at VV polarization. The ocean surface part of our model was based on Bragg resonance between the sea surface waves and the radiative waves; the sea surface waves were simulated by a wave spectrum, and therefore a particular scale of the ocean surface is needed to cover enough wave scales. Therefore, we calibrated the SAR image and then averaged the spatial resolution to 1 km (shown in Figure 4) with the boxcar averaging method. Moreover, with the averaging, the SAR speckle noise is almost removed. The calibration process is also a methodology to transfer the SAR image pixels to latitude and longitude spatial location information, using the transfer function given by ESA.

3.2. SFMR-Measured Hurricane Wind and Rain

At the two SAR imaging times, we also obtained wind speeds and rain rates, as measured by the stepped-frequency microwave radiometer (SFMR) on board the WP-3-D research aircraft, which is employed for NOAA's operational surface wind and rain measurements [*Uhlhorn and Black*, 2003]. SFMR provides along-track mapping of wind speeds at relatively high spatial (1.5 km) and temporal (1 Hz) resolutions. These winds are well validated by measurements from dropwindsondes, each equipped with GPS. The RMS error for SFMR measurements is less than ∼4 m/s at the surface and less than ∼5 m/s at 10 m height [*Uhlhorn et al.*, 2007]. With six frequencies between 4.5 and 7.2 GHz used in the SFMR, the rain rate is also inferred with the wind speed. The rain rate error is less than ∼5 mm/h, after algorithm correction and error analysis

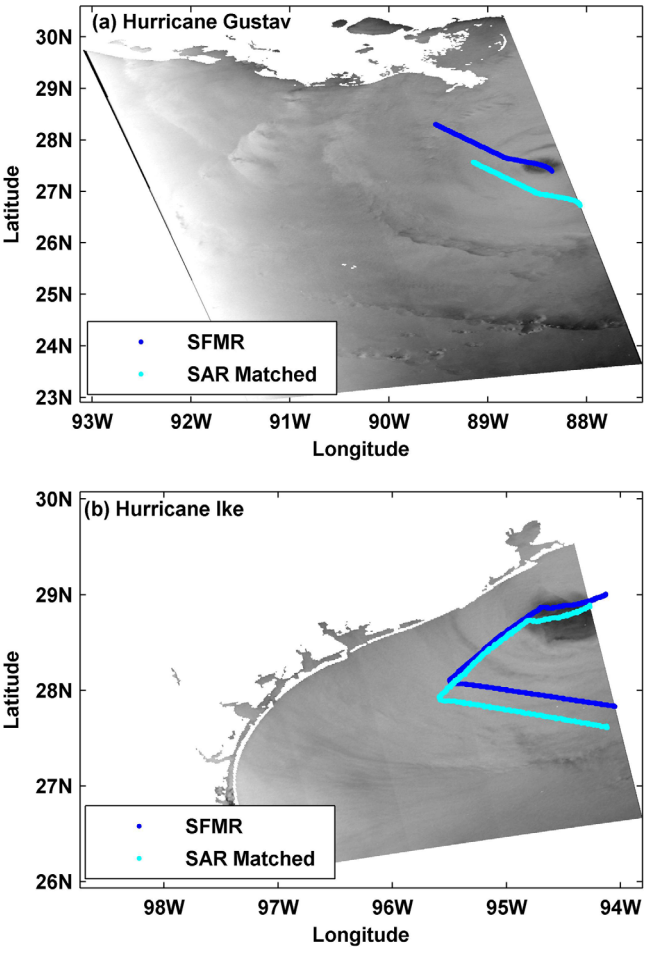

Figure 4. *Envisat* SAR images for: (a) Hurricane Gustav (03:59 UTC, 1 September 2008) and (b) Hurricane Ike (04:23 UTC, 13 September 2008). And the positions of SFMR adopted here were displayed in blue points as well as the SAR data matched up in cyan points.

[*Jiang et al.*, 2006]. Along the flight track (blue dots in Figure 4), longitude, latitude, sea surface wind speed, and rain rate are measured at the same time.

3.3. Matchup SAR and SFMR for Moving Hurricanes

SFMR data selected here were collected during a flight that lasted 1 h but two SAR image were captured almost instantaneously. During this 1 h, the hurricane also moves. Therefore, our matchup process here was carried out to remove the effect of the relative movement between the aircraft carrying the SFMR and the hurricane. Moreover, we assume that the hurricane moves linearly along the Best Track (BT) during this 1 h. For the hurricane moving continuously along a trajectory, we map the hurricane center observed by SAR to the BT position at each SFMR measurement time. The center locations of BT and of SAR hurricane images detected by *Li et al.* [2013] were adopted, as shown in Table 1. To simplify the process, we assume that the hurricane moves linearly between two BT locations without rotation.

For each selected set of wind speeds and rain rates measured by SFMR, the mapping procedure consists of the following steps: (1) interpolate the BT center locations to the time of the SFMR observation; (2) move the SAR image to colocate the SAR center and the interpolated BT center; (3) determine whether the SFMR data set is within the *mapped* SAR image, or not; (4) if yes, the data set from the SFMR and the NRCS for the same location in the mapped SAR image are considered to be *matched* (cyan dots shown in Figure 4). As shown in Figure 5, there are 296 matchups of wind speed, rain rate, and NRCS. The rain rates are between 10 and 35 mm/h, wind speeds are from 25 to 45 m/s, and the NRCSs are between −10 and −5 dB.

3.4. Validation Results

To model the volume scattering and attenuation due to rain in the atmospheric column, three-dimensional rain rates are needed, which are difficult to measure. Therefore, we modeled the NRCSs for the matched data sets using only the ocean surface part. The model results with: (a) wind only (Figure 6a) and (b) with

Table 1. Hurricane Center Information of SAR and Related Best Track Estimates

		SAR			Best Track		
Name	Date	Time	Latitude	Longitude	Time	Latitude	Longitude
Gustav	1 Sep 2008	03:59	27.0°N	88.4°W	00:00	26.9°N	87.7°W
					06:00	27.9°N	89.0°W
Ike	13 Sep 2008	04:23	28.0°N	94.6°W	00:00	28.3°N	94.0°W
					06:00	29.1°N	94.6°W

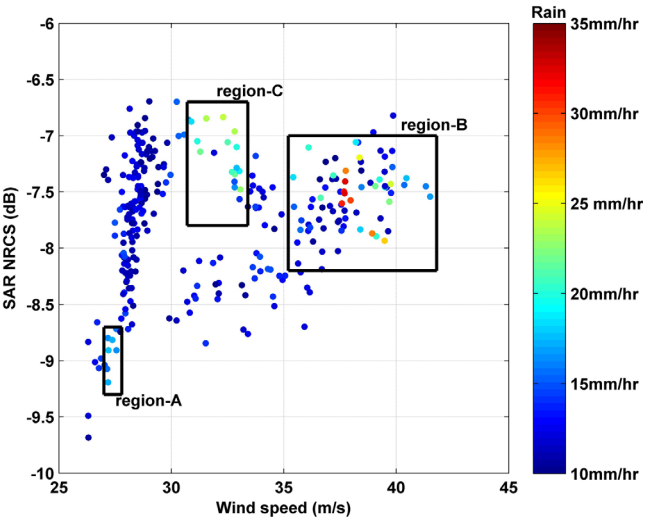

Figure 5. The collected matchup data sets: wind speed and rain rate measured by SFMR, as well as NRCS observed by SAR.

both wind and rain (Figure 6b) are plotted against the matched data set. For the wind-only model results, the comparison has a bias of 0.71 dB, a standard deviation of 0.60 dB, and correlation coefficient of 80.9%. When the rain effect is taken into account, the simulation results improved; the bias is 0.20 dB with a standard deviation of 0.54 dB and correlation coefficient is 81.9%. In the comparisons shown in Figure 6, near the SAR NRCSs at about −9.0 dB, the rain rate is about 20 mm/h (hereafter defined as region-A), and our composite model appears to simulate the attenuation of the NRCSs due to rain very well. When the NRCSs are about −7.7 dB, as observed by SAR, the effect of heavy rain is about 30 mm/h (hereafter defined as region-B), which also appears to be modeled appropriately. However, when the SAR NRCSs is −7.0 dB with rain rate of 20 mm/h (defined as region-C), this case is not simulated very well, although the results presented in Figure 6b are still better than those of Figure 6a. In terms of winds, Figure 5 implies that the wind speeds are about 27.5 m/s for region-A and from 35.0 to 42.0 m/s for region-B, and resulting SAR NRCSs are reasonably well simulated. The disagreement between simulated and measured NRCSs occurs near wind speeds of about 32.0 m/s. This demonstrates that the bias of region-B is not caused by the model saturation due to high wind speeds. A possible reason may be the asymmetry and rotational motion of the hurricane.

4. Mechanisms for Rain Effects on SAR Hurricane Observations

The modeling approach used here consists of modifying the parameterization for a wind wave spectra to include: (a) rain-induced turbulent damping and the enhancement of small gravity and gravity capillary waves due to the presence of ring waves, (b) the attenuation and volume scattering due to raindrops in the atmosphere, then (c) analyzing the backscatter caused by rain on both the ocean surface and in the atmosphere. In total, there are four possible ways that rain can affect the NRCS: (1) rain droplets can attenuate the RADAR signal crossing the atmosphere; (2) rain droplets can cause volume scattering and thus increase the backscattering NRCS; (3) the radar waves can experience diffraction on rain products on the ocean surface including craters, crowns, and stalks; (4) rain changes the ocean surface waves as generated and driven by wind. In this paper, the former two ways are summarized as the atmosphere part, and the latter two ways, as the ocean surface part.

4.1. Volume Scattering and Attenuation

Based on the atmosphere model, the rain effect in the atmosphere is described by:

$$\Delta\sigma_0(dB) = 10 \cdot lg(\sigma_{surf}\alpha_{atm} + \sigma_{atm}) - 10 \cdot lg(\sigma_{surf}) \tag{17}$$

Therefore, C-band NRCS affected by rain in the atmosphere is simulated and shown in Figure 7 for the rain rates of 10, 30, and 50 mm/h, respectively, with the assumption that rain rates were not changing along the radiative incidence track. The VV-polarized hurricane measurements, which are mostly between −18 and −5 dB for winds above 5 m/s, are probably attenuated by the rain in the atmosphere; Figure 7 suggests that the effects of attenuation and volume backscattering in the atmosphere are less than 1 dB, even with a rain rate of 50 mm/h along the incidence track. As shown in Figures 8 and 9, when the NRCS is between −18 and −5 dB, the wind speed varies from 5 to 50 m/s. Moreover, the rain rate is not always the same along the entire radiative incidence track, as is often assumed in a hurricane; therefore, the real effect of rain in atmosphere should be less than the results simulated (with assuming a maximum rain rate of

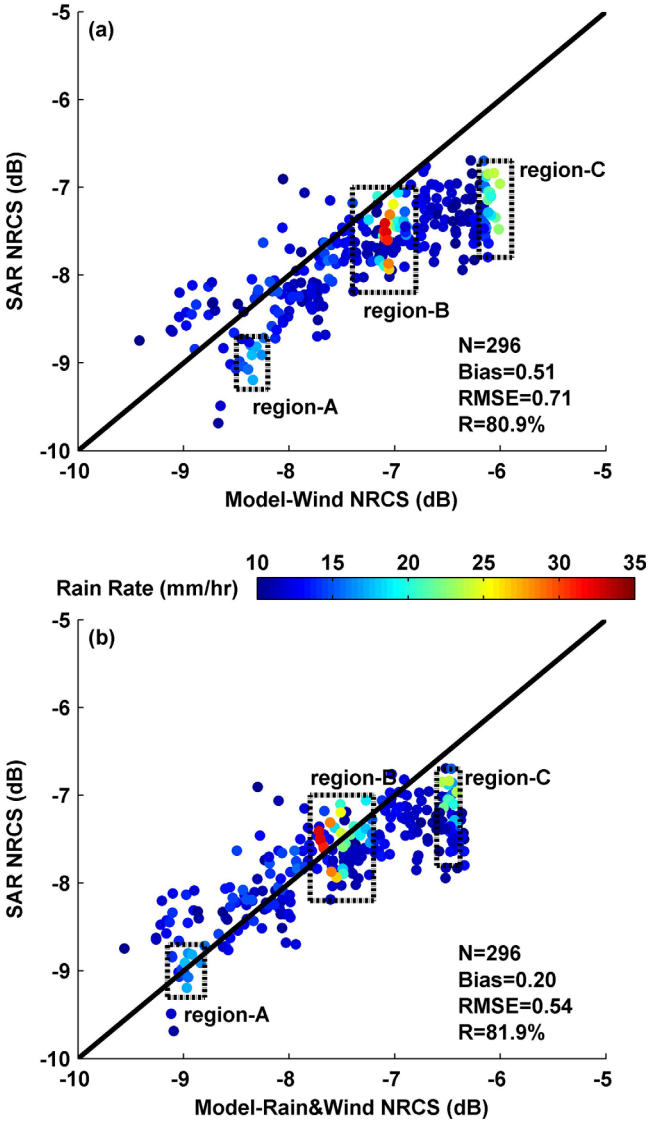

Figure 6. Comparisons between simulated NRCS induced by the ocean surface part of the composite model and the ASAR observed NRCS: (a) simulation with only wind, and (b) simulation with wind and rain.

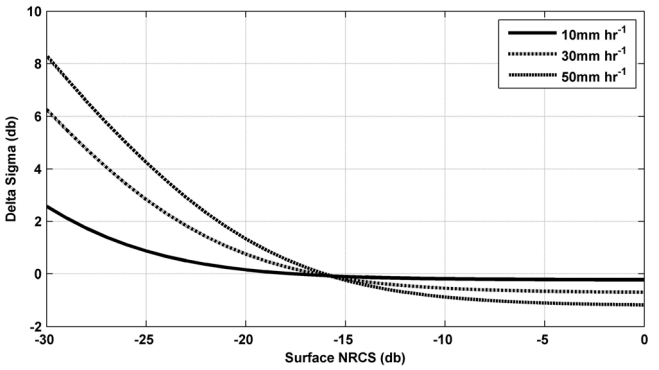

Figure 7. Rain effects on attenuation and volume backscattering in the atmosphere as a function of the sea surface backscatter with three different rain rates.

50 mm/h). Hence, we conclude that the atmospheric part can be neglected for C-band VV polarization in the hurricane observations. When the sea surface backscattering NRCS is less than −15 dB, representing wind speeds of about 40 m/s for the cross polarization (Figures10 and 11), the NRCS is enhanced because of the volume scattering, due to rain.

4.2. Rain Products Diffraction

For C-band VV-polarized SAR observations, the dependency of the NRCSs on the wind speed and the SAR geometries (e.g., incidence angle and azimuth angle with respect to wind direction) is generally expressed by the GMF, such as the two-scale model [*Wackerman et al.*, 2002] and CMOD5 for neutral winds (CMOD5.N) [*Hersbach et al.*, 2007, *Hersbach*, 2010]. For cross-polarization images (VH, HV), an empirical function denoted C-2PO was developed by *Zhang and Perrie* [2012]. For the HH-polarization, no well-developed empirical function exists and the widely used approach is to develop a hybrid model function consisting of one of the GMFs and a polarization ratio [e.g., *Zhang et al.*, 2011; *Nunziata et al.*, 2014]. However, HH-polarization SAR images are not discussed in this study.

We compare model results with the empirical functions, considering only the wind-induced KHCC wave spectrum for the VV-polarization SAR images and the cross-polarization SAR images. Figures 8 (upwind) and 9 (crosswind) present the VV-polarized NRCSs simulated by this model, in comparison with results from CMOD5.N. One can see that the simulated NRCS results are close to those from CMOD5.N for both the upwind and crosswind cases, illustrating that this model can reliably simulate the NRCS, with respect to wind-generated KHCC wave spectra.

However, for cross polarizations, we only simulate the modulation of NRCS by ocean wind without considering rain's effect. The wind-induced NRCS modulations in both upwind (Figure 10) and crosswind (Figure 11) cases are much smaller than the results given by

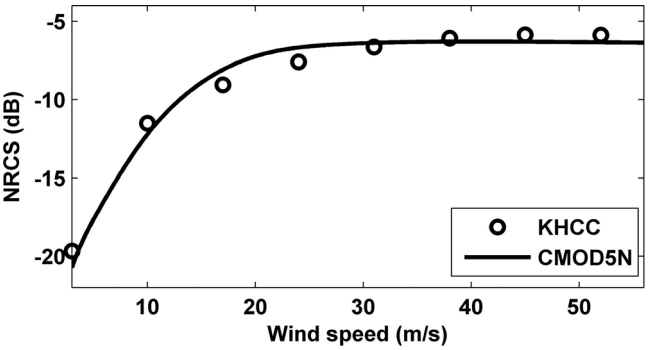

Figure 8. NRCS as a function of the wind speed, comparing the composite model only, with KHCC wind wave spectrum (black circles) and the CMOD5N function. The incidence angle is 38°, and the relative wind direction is 0° (upwind) for C-band VV-polarization.

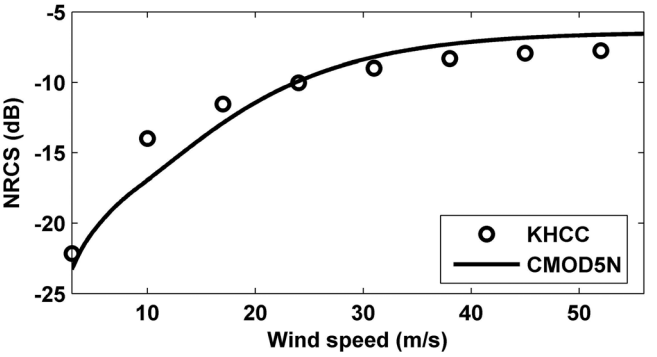

Figure 9. NRCS as a function of the wind speed for the comparison between the composed model only with KHCC wind wave spectrum (black circles) and the CMOD5N function. The incidence angle is 38°, and the relative wind direction is 90° (crosswind) for C-band VV-polarization.

the C-2PO model. The reason is that the Bragg model is not suitable for wind-induced NRCS simulation for the cross-pol imagery, and certainly does not include the rain's effect. Therefore, the rain's effect on ocean wave was not simulated for the cross-pol signal in this study. The underestimated NRCSs values may be caused by non-Bragg scattering, including specular reflection and diffraction of radio waves on sharp wedges of wave crest breaks [*Kalmykov and Pustovoytenko*, 1976]. The non-Bragg scattering is not simulated in this model and is not related to polarizations. However, the VV-polarized NRCS values are much larger than those of cross-polarization images, with the same wind speed, which is evident, comparing Figures 8 and 9 with Figures 10 and 11. Hence, although the non-Bragg scattering impacts on the cross polarization are significant, the impacts on the VV-polarization are slight. Just as for the crest breaks, we speculated that the diffraction of radio waves on the sharp wedges of craters, crowns, and stalks produced by rain colliding with the sea surface can be neglected for C-band VV polarized SAR hurricane observations, but should be important for the cross-polarization images.

4.3. Changes on the Wind-Induced Waves

We have found that the previous three mechanisms for the rain effects on the NRCS can be neglected for C-band VV polarized SAR hurricane observations. Here we also consider the impacts of rain on wind-generated waves. Based on the validation in section 3.2, we simulated NRCSs with the rain damped wave spectrum, in comparison with the rain changed wave spectrum (that is, wave spectrum damped by rain and adding the ring waves generated by rain) for the C-band VV-polarization shown in Figure 12 for upwind wind cases, and Figure 13, for crosswind cases. Therefore, even with the rain-induced ring waves, the NRCSs are also attenuated by the precipitation, for both upwind (Figure12) and crosswind (Figure 13) directions. However, the attenuation of the NRCSs values due to the rain damping effect decreases, with increasing wind speeds. Conversely, the total rain effect on the sea surface

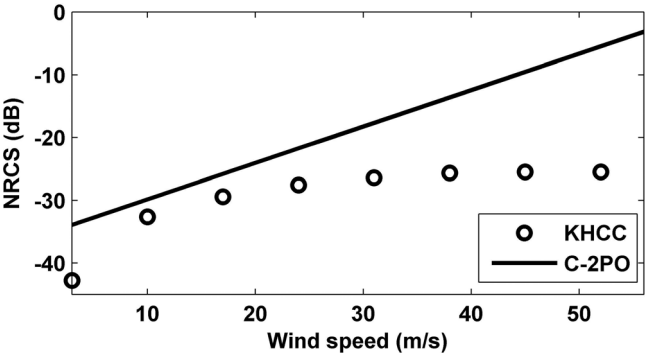

Figure 10. NRCS as a function of the wind speed for the comparison between the model only with KHCC wind wave spectrum (black circle) and the C-2PO function. The incidence angle is 38°, and the relative wind direction is 0° (upwind) for C-band cross polarization.

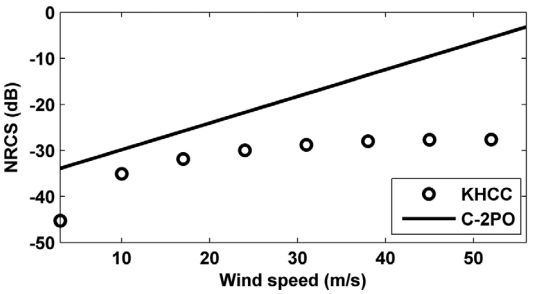

Figure 11. NRCS as a function of the wind speed for the comparison between the models only with KHCC wind wave spectrum (black circles) and the C-2PO function. The incidence angle is 38°, and the relative wind direction is 90° (crosswind) for C-band cross polarization.

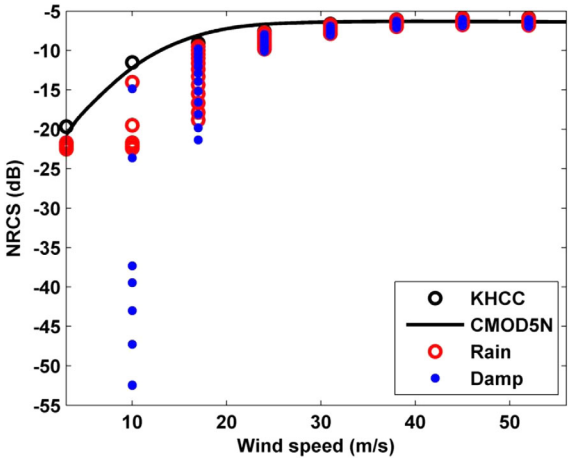

Figure 12. Simulated NRCSs with different wave spectra: only with wind wave spectrum (black circles), with the damped wind wave spectrum (blue points), with the damped wind wave and ring wave spectra (red circles), and the CMOD5.N function (solid line). The incidence angle is 38°, and the relative wind direction is 0° (upwind) for C-band VV-polarization. From upper to lower limits on the plot, rain rates are from 5 to 60 mm/s with the increments of 5 mm/s.

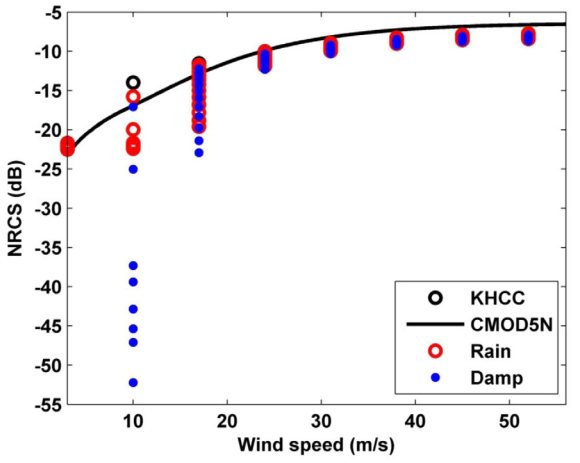

Figure 13. Simulated NRCSs as Figure 12 but for crosswind (relative wind direction is 90°).

(wind wave damped by rain and the ring waves generated by rain) increases, with decreasing or during low wind speeds (<10 m/s), but decreases for increasing, moderate and high wind speeds.

5. Conclusions

In this paper, five possible mechanisms for the rain effects on the spaceborne C-band SAR hurricane observations are considered: (1) attenuation and (2) volume backscattering for the microwave transfer in atmosphere, as well as (3) rain-induced damping to the wind waves and (4) rain-generated ring waves on the ocean surface, and (5) diffraction on the sharp edges of rain products. The first four mechanisms are simulated by a composite model, and the fifth mechanism was discussed. Comparisons between the observed NRCSs and the atmosphere part of our model imply that two possible effects in the atmosphere can be neglected for C-band VV-polarization SAR hurricane observations. However, the atmosphere part should be important at very low wind speed and the VV-polarized NRCS will be increased for the volume backscattering. Thus, we speculated that the diffraction of radio waves on craters, crowns, and stalks, induced by rain on the ocean surface can be neglected for C-band VV-polarization, and that the NRCSs are essentially affected only by wind and can be simulated well for C-band VV-polarization data without including the diffraction of the radar by the sharp wedges of wave breaking but not well for the cross-polarization data (Figures 10 and 11). However, the mechanism of diffraction on the sharp wedges of wave breaking and rain products needs to be further modeled to validate this speculation. Our composite model was validated with the matchup of observations of wind speed and rain rate from the SFMR data as well as the NRCSs and incidence angles of C-band VV-polarization SAR data over two hurricanes.

Therefore, the most important mechanism for the rain effect on the C-band VV polarized SAR hurricane observations is through the influence of waves on the ocean surface. Moreover, the non-Bragg parameterization will be added to our model to study whether or not it can explain the gaps in the C-2PO results, in future studies.

Acknowledgments

The authors thank the European Space Agency's (ESA) for providing Envisat VV-polarization SAR hurricane imagery, and NOAA HRD for supplying SFMR data, which can be downloaded at http://www.aoml.noaa.gov/hrd/project2005/sfmr.html. This research work was supported by National Science Foundation of China, the Chinese National High Technology Research and Development (863) Program grant 2013AA09A505, and National Program on Global Change and Air-Sea Interaction grant GASI-IPOVAI-04. We thank three anonymous reviewers for their constructive comments that helped us improve this paper. The views, opinions, and findings contained in this report are those of the authors and should not be construed as an official NOAA or U.S. government position, policy, or decision.

References

Bass, F., I. Fuks, A. Kalmykov, I. Ostrovsky, and A. Rosenberg (1968), Very high frequency radiowave scattering by a disturbed sea surface part II: Scattering from an actual sea surface, *IEEE Trans. Antennas Propag.*, *16*(5), 560–568, doi:10.1109/TAP.1968.1139244.

Contreras, R. F., and W. J. Plant (2006), Surface effect of rain on microwave backscatter from the ocean: Measurements and modeling, *J. Geophys. Res.*, *111*, C08019, doi:10.1029/2005JC003356.

Cox, C., and W. Munk (1954), Statistics of the sea surface derived from sun glitter, *J. Mar. Res.*, *13*(2), 198–227.

Du, Y., and P. W. Vachon (2003), Characterization of hurricane eyes in RADARSAT-1 images with wavelet analysis, *Can. J. Remote Sens.*, *29*(4), 491–498, doi:10.5589/m03-020.

Elfouhaily, T., B. Chapron, K. Katsaros, and D. Vandemark (1997), A unified directional spectrum for long and short wind-driven waves, *J. Geophys. Res.*, *102*(C7), 15,781-15,796, doi:10.1029/97JC00467.

Friedman, K., and X. Li (2000), Storm patterns over the ocean with wide swath SAR, *Johns Hopkins APL Tech. Dig.*, *21*, 80–85.

Fu, L. L., and B. Holt (1982), *Seasat Views Oceans and Sea Ice With Synthetic Aperture Radar*, National Aeronautics and Space Administration (NASA), Jet Propulsion Laboratory (JPL) Publication 81–120, Pasadena, Calif.

Hersbach, H. (2010), Comparison of C-band scatterometer CMOD5. N equivalent neutral winds with ECMWF, *J. Atmos. Oceanic Technol.*, *27*(4), 721–736, doi:10.1175/2009JTECHO698.1.

Hersbach, H., A. Stoffelen, and S. de Haan (2007), An improved C-band scatterometer ocean geophysical model function: CMOD5, *J. Geophys. Res.*, *112*, C03006, doi:10.1029/2006JC003743.

Hwang, P. A., and W. J. Plant (2010), An analysis of the effects of swell and surface roughness spectra on microwave backscatter from the ocean, *J. Geophys. Res.*, *115*, C04014, doi:10.1029/2009JC005558.

Hwang, P. A., B. Zhang, J. V. Toporkov, and W. Perrie (2010), Comparison of composite Bragg theory and quad-polarization radar backscatter from RADARSAT-2: With applications to wave breaking and high wind retrieval, *J. Geophys. Res.*, *115*, C08019, doi:10.1029/2009JC005995.

Jiang, H., P. G. Black, E. J. Zipser, F. D. Marks Jr., and E. W. Uhlhorn (2006), Validation of rain-rate estimation in hurricanes from the stepped frequency microwave radiometer: Algorithm correction and error analysis, *J. Atmos. Sci.*, *63*(1), 252–267, doi:10.1175/JAS3605.1.

Jin, S., S. Wang, and X. Li (2014), Typhoon eye extraction with an automatic SAR image segmentation method, *Int. J. Remote Sens.*, *35*(11–12), 3978–3993, doi:10.1080/01431161.2014.916447.

Kalmykov, A. I., and V. V. Pustovoytenko (1976), On polarization features of radio signals scattered from the sea surface at small grazing angles, *J. Geophys. Res.*, *81*(12), 1960–1964, doi:10.1029/JC081i012p01960.

Kudryavtsev, V., D. Hauser, G. Caudal, and B. Chapron (2003), A semiempirical model of the normalized radar cross-section of the sea surface: 1. Background model, *J. Geophys. Res.*, *108*(C3), 8054, doi:10.1029/2001JC001003.

Kudryavtsev, V., I. Kozlov, B. Chapron, and J. A. Johannessen (2014), Quad-polarization SAR features of ocean currents, *J. Geophys. Res. Oceans*, *119*, 6046–6065, doi:10.1002/2014JC010173.

Le Méhauté, B. (1988), Gravity–capillary rings generated by water drops, *J. Fluid Mech.*, *197*, 415–427, doi:10.1017/S0022112088003301.

Li, X. (2015), The first Sentinel-1 SAR image of a Typhoon, *Acta Oceanol. Sin.*, *34*(1), 1–2, doi:10.1007/s13131-015-0589-8.

Li, X., W. G. Pichel, M. X. He, S. Y. Wu, K. S. Friedman, P. Clemente-Colón, and C. Zhao (2002), Observation of hurricane-generated ocean swell refraction at the Gulf Stream north wall with the RADARSAT-1 synthetic aperture radar, *IEEE Trans. Geosci. Remote Sens.*, 40(10), 2131–2142, doi:10.1109/TGRS.2002.802474.

Li, X., J. A. Zhang, X. Yang, W. G. Pichel, M. DeMaria, D. Long, and Z. Li (2013), Tropical cyclone morphology from spaceborne synthetic aperture radar, *Bull. Am. Meteorol. Soc.*, *94*(2), 215–230, doi:10.1175/BAMS-D-11-00211.1.

Marshall, J. S., and W. M. Palmer (1948), The distribution of raindrops with size, *J. Meteorol.*, *5*, 165–166, doi:10.1175/1520-0469(1948)005 <0165:TDORWS>2.0.CO;2.

Nie, C., and D. G. Long (2007), A C-band wind/rain backscatter model, *IEEE Trans. Geosci. Remote Sens.*, *45*(3), 621–631, doi:10.1109/TGRS.2006.888457.

Nunziata, F., M. Migliaccio, X. Li, and X. Ding (2014), Coastline extraction using dual-polarimetric COSMO-SkyMed PingPong mode SAR data, *IEEE Trans. Geosci. Remote Sens.*, *11*(1), 104–108, doi:10.1109/LGRS.2013.2247561.

Nystuen, J. A. (1990), A note on the attenuation of surface gravity waves by rainfall, *J. Geophys. Res.*, *95*(C10), 18,353-18,355, doi:10.1029/JC095iC10p18353.

Plant, W. J. (1990), Bragg scattering of electromagnetic waves from the air/sea interface, in *Surface Waves and Fluxes*, pp. 41–108, Springer, Dordrecht, Netherlands.

Reppucci, A., S. Lehner, J. Schulz-Stellenfleth, and S. Brusch (2010), Tropical cyclone intensity estimated from wide-swath SAR images, *IEEE Trans. Geosci. Remote Sens.*, *48*(4), 1639–1649, doi:10.1109/TGRS.2009.2037143.

Tsimplis, M. N. (1992), The effect of rain in calming the sea, *J. Phys. Oceanogr.*, *22*(4), 404–412, doi:10.1175/1520-0485(1992)022 <0404:TEORIC>2.0.CO;2.

Uhlhorn, E. W., and P. G. Black (2003), Verification of remotely sensed sea surface winds in hurricanes, *J. Atmos. Oceanic Technol.*, *20*(1), 99–116, doi:10.1175/1520-0426(2003)020>0099:VORSSS>2.0.CO;2.

Uhlhorn, E. W., P. G. Black, J. L. Franklin, M. Goodberlet, J. Carswell, and A. S. Goldstein (2007), Hurricane surface wind measurements from an operational stepped frequency microwave radiometer, *Mon. Weather Rev.*, *135*(9), 3070–3085, doi:10.1175/MWR3454.1.

Valenzuela, G. R. (1978), Theories for the interaction of electromagnetic and oceanic waves—A review, *Boundary Layer Meteorol.*, *13*(1-4), 61–85, doi:10.1007/BF00913863.

Valenzuela, G. R. (1968), Scattering of electromagnetic waves from a tilted slightly rough surface, *Radio Sci.*, *3*, 1057–1066.

Wackerman, C. C., P. Clemente-Colon, W. Pichel, and X. Li (2002), A two-scale model to predict C-band VV and HH normalized radar cross section values over the ocean, *Can. J. Remote Sens.*, *28*(3), 367–384, doi:10.5589/m02-044.

Wright, J. (1966), Backscattering from capillary waves with application to sea clutter. *Antennas and Propagation, IEEE Trans. Antennas Propag.*, *14*(6), 749–754, doi:10.1109/TAP.1966.1138799.

Xu, F., X. Li, P. Wang, J. Yang, W. G. Pichel, and Y. Q. Jin (2015), A backscattering model of rainfall over rough sea surface for synthetic aperture radar, *IEEE Trans. Geosci. Remote Sens.*, *53*(6), 3042–3054, doi:10.1109/TGRS.2014.2367654.

Zhang, B., and W. Perrie (2012), Cross-polarized synthetic aperture radar: A new potential measurement technique for hurricanes, *Bull. Am. Meteorol. Soc.*, *93*(4), 531–541, doi:10.1175/BAMS-D-11-00001.1.

Zhang, B., W. Perrie, and Y. He (2011), Wind speed retrieval from RADARSAT-2 quad-polarization images using a new polarization model, *J. Geophys. Res.*, *116*, C08008, doi:10.1029/2010JC006522.

Zhang, G., B. Zhang, W. Perrie, Q. Xu, and Y. He (2014), A hurricane tangential wind profile estimation method for C-band cross-polarization SAR, *IEEE Trans. Geosci. Remote Sens.*, *52*(11), 7186–7194, doi:10.1109/TGRS.2014.2308839.

Zheng, G., J. Yang, A. K. Liu, X. Li, W. G. Pichel, and S. He (2015), Comparison of typhoon centers from SAR and IR Images and those from best track datasets, *IEEE Trans. Geosci. Remote Sens.*, doi:10.1109/TGRS.2015.2472282, in press.

Zhou, X., X. Yang, Z. Li, Y. Yu, H. Bi, S. Ma, and X. Li (2013), Estimation of tropical cyclone parameters and wind fields from SAR images, *Sci. China Earth Sci.*, *56*(11), 1977–1987, doi:10.1007/s11430-013-4633-2.